Janus monolayers of transition metal dichalcogenides

Ang-Yu Lu[1†], Hanyu Zhu[2†], Jun Xiao[2†], Chih-Piao Chuu[3], Yimo Han[4], Ming-Hui Chiu[1], Chia-Chin Cheng[5,6], Chih-Wen Yang[1], Kung-Hwa Wei[6], Yiming Yang[7,8], Yuan Wang[2,8], Dimosthenis Sokaras[9], Dennis Nordlund[9], Peidong Yang[7,8], David A. Muller[4,10], Mei-Yin Chou[3,11,12], Xiang Zhang[2,8]★ and Lain-Jong Li[1]★

Structural symmetry-breaking plays a crucial role in determining the electronic band structures of two-dimensional materials. Tremendous efforts have been devoted to breaking the in-plane symmetry of graphene with electric fields on AB-stacked bilayers[1,2] or stacked van der Waals heterostructures[3,4]. In contrast, transition metal dichalcogenide monolayers are semiconductors with intrinsic in-plane asymmetry, leading to direct electronic bandgaps, distinctive optical properties and great potential in optoelectronics[5,6]. Apart from their in-plane inversion asymmetry, an additional degree of freedom allowing spin manipulation can be induced by breaking the out-of-plane mirror symmetry with external electric fields[7,8] or, as theoretically proposed, with an asymmetric out-of-plane structural configuration[9]. Here, we report a synthetic strategy to grow Janus monolayers of transition metal dichalcogenides breaking the out-of-plane structural symmetry. In particular, based on a MoS_2 monolayer, we fully replace the top-layer S with Se atoms. We confirm the Janus structure of MoSSe directly by means of scanning transmission electron microscopy and energy-dependent X-ray photoelectron spectroscopy, and prove the existence of vertical dipoles by second harmonic generation and piezoresponse force microscopy measurements.

We first prepare single-crystalline triangular molybdenum disulfide (MoS_2) monolayers on *c*-plane sapphire substrates using chemical vapour deposition[10,11], then strip off the top-layer sulfur atoms and replace them with hydrogen atoms using a remote hydrogen plasma (Fig. 1a). Without breaking the vacuum, the subsequent thermal selenization allows Se to replace the H atoms, forming a structurally stable Janus MoSSe monolayer in which the Mo atoms are covalently bonded to underlying S and top-layer Se atoms. Optical microscope images for the monolayer at each stage are presented in Fig. 1a, where the stripped MoS_2 (MoSH) is shown to retain its triangular shape. Atomic force microscope images reveal an apparent change in the cross-sectional height from 1.0 nm for pristine MoS_2 to 0.7–0.8 nm for MoSH and 1.1 nm for Janus MoSSe. The reduced thickness after H_2-plasma indicates the successful S-stripping. Our first-principles calculations further predict that the H_2-plasma-treated MoS_2 should generate

hydrogenated MoS with nearly full H-coverage (MoSH), due to the large absorption energy of H atoms at the vacancy sites (~1 eV per H atom) (see Supplementary Section 'Theoretical calculation'). The plasma power needs to be at an optimum value to break the surface Mo–S bonds but still preserve the underlying two-dimensional Mo–S structure. In this respect, the remote plasma produced from light molecules (hydrogen) works better than that from heavy molecules such as argon plasma[12], which easily destroys the entire two-dimensional structure (as shown in Supplementary Fig. 1a). The selenization temperature also plays a critical role. The substrate temperature needs to be higher than 350 °C for Mo–Se bond formation but not higher than 450 °C, where the two-dimensional structure becomes unstable and holes appears in the monolayer (Supplementary Fig. 1b). When the temperature is higher than 600 °C, randomized MoSSe alloy structures are obtained, and the Se and S are mixed in a disordered arrangement at both the top and bottom surfaces, reaching a state of maximum entropy with a thermodynamically favoured structure in an Ar/H_2 environment, consistent with previous reports[13,14]. Hence, the key to the synthetic strategy for Janus MoSSe is to control the reaction by kinetics rather than thermodynamics.

Figure 1b shows that the intensities of Raman out-of-plane A_1 (406 cm^{-1}) and in-plane E′ (387 cm^{-1}) modes for a MoS_2 monolayer decrease (curve for 5 min stripping) and eventually vanish (curve for 20 min stripping) with increasing stripping time, agreeing well with the calculated phonon dispersion of the expected MoSH structure (Supplementary Fig. 3a). Note that we perform the subsequent thermal sulfurization or selenization only for the samples not showing any Raman A_1 and E′ peaks. Interestingly, the A_1 and E′ peaks appear again after sulfurization, indicating the recovery of MoS_2 monolayers from MoSH and the reversibility of this process. When we perform the selenization for MoSH, the A_1 peak shifts to 288 cm^{-1} from the original 406 cm^{-1}, and the E′ peak shifts to 355 cm^{-1} from 387 cm^{-1} in MoS_2. These peaks match well with the two major phonon energies predicted in Supplementary Fig. 3b,c. The shift of the A_1 frequency is caused by the out-of-plane symmetry change upon selenization, while the shift of the E′ mode is related to a change in the lattice constant. Figure 1c shows that the optical gap of a pristine MoS_2 monolayer

[1]Physical Sciences and Engineering Division, King Abdullah University of Science and Technology, Thuwal, 23955-6900, Saudi Arabia. [2]NSF Nanoscale Science and Engineering Center, University of California, Berkeley, California 94720, USA. [3]Institute of Atomic and Molecular Sciences, Academia Sinica, Taipei 10617, Taiwan. [4]School of Applied & Engineering Physics, Cornell University, Ithaca, New York 14850, USA. [5]Research Center for Applied Sciences, Academia Sinica, Taipei 10617, Taiwan. [6]Department of Material Science and Engineering, National Chiao Tung University, Hsinchu 300, Taiwan. [7]Department of Chemistry, University of California, Berkeley, California 94720, USA. [8]Materials Sciences Division, Lawrence Berkeley National Laboratory, Berkeley, California 94720, USA. [9]SLAC National Accelerator Laboratory, 2575 Sand Hill Road, Menlo Park, California 94025, USA. [10]Kavli Institute at Cornell for Nanoscale Science, Ithaca, New York 14853, USA. [11]Department of Physics, National Taiwan University, Taipei 10617, Taiwan. [12]School of Physics, Georgia Institute of Technology, Atlanta, Georgia 30332, USA. †These authors contributed equally to this work. *e-mail: xiang@berkeley.edu; lance.li@kaust.edu.sa
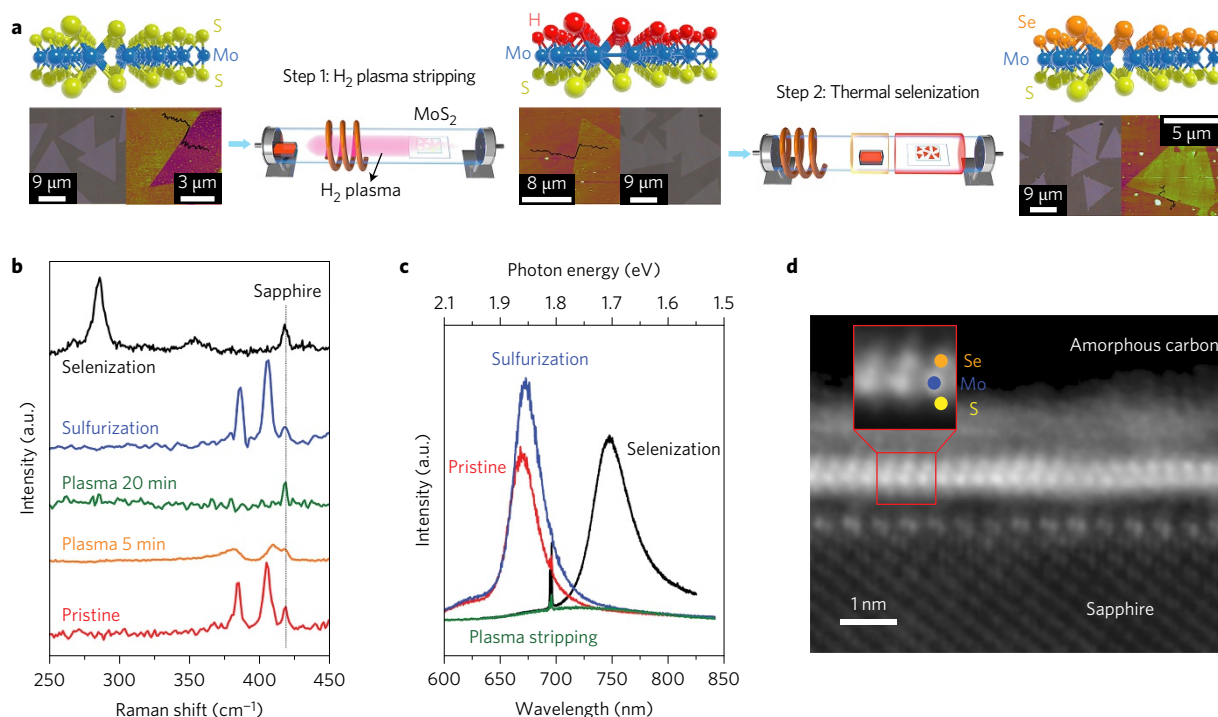
Figure 1 | Synthesis of the Janus MoSSe monolayer. a, A MoS$_2$ monolayer grown by chemical vapour deposition was exposed to H$_2$ plasma to strip the top-layer S. The plasma was then switched off and a quartz boat loaded with Se powder was moved next to the sample without breaking the vacuum. Se powders were then thermally vaporized to achieve selenization and complete the synthesis of Janus MoSSe monolayers. Optical microscopy and atomic force microscopy images for each structure are shown below the corresponding molecular model. **b,c**, Raman characteristics (**b**) and photoluminescence results (**c**) for the MoS$_2$ and those after H$_2$ plasma treatment, sulfurization and selenization. **d**, Annular dark-field scanning transmission electron microscopy image of the sample cross-section, showing the asymmetric MoSSe monolayer structure with Se (orange) on top and S (yellow) at the bottom of the Mo atoms (blue).

at 1.88 eV disappears after S-stripping, agreeing with the metallic property of the MoSH predicted by density functional theory calculations (Supplementary Fig. 4). The photoluminescence for the MoSH samples recovers to that of MoS$_2$ after sulfurization, consistent with the observation in Raman measurements. The optical gap for the Janus MoSSe monolayer is at 1.68 eV, close to the average of the optical gaps of MoS$_2$ and MoSe$_2$, and consistent with the calculated energy gap in these monolayers (Supplementary Fig. 5a). Note that the major effect of mirror symmetry breaking is Rashba spin splitting, where the valence band maxima at the Γ point displays a horizontal shift in E–k dispersion and is governed by out-of-plane d_{z^2} orbitals. However, the photoluminescence energy is dominated by the valence band maxima at the K point, which is determined by the in-plane $d_{x^2-y^2}/d_{xy}$ orbital; hence, the photoluminescence energy of Janus MoSSe seems indistinguishable from that of the randomized MoSSe monolayer (see Supplementary Fig. 5b for details). Meanwhile, we examined the helicity of the Janus MoSSe monolayer by measuring circularly polarized photoluminescence (Supplementary Fig. 6a,b), a typical way to identify the valley degree of freedom[15,16]. The helicity at the emission peak is ~9% at room temperature and 50% at 90 K, which confirms the preservation of valley properties and is consistent with the calculation of valley-dependent Berry curvature (Supplementary Fig. 6c). Figure 1d presents an annular dark-field scanning transmission electron microscopy image of a cross-section of the Janus MoSSe monolayer. Since the image contrast is proportional to the square of the atomic number, the bottom S and top Se atoms are clearly distinguishable, confirming the success of our proposed synthetic approach.

The atomic percentage of Se atoms in the top layer of the Janus MoSSe monolayer was determined to be 96.2% by energy-dispersive

X-ray spectroscopy and transmission electron microscopy measurements (Supplementary Fig. 8 and Supplementary Table 3). We also used energy-dependent X-ray photoelectron spectroscopy to probe the asymmetric structure of the MoSSe monolayers, where the photon energy varies from 250 to 1,150 eV and the incident beam angle is 20°, as shown in Fig. 2a. In general, the doublet peaks originating from the S 2p and Se 3p orbitals for a MoSSe monolayer appear at around (162.4; 163.6) eV and (161.3; 167.1) eV, respectively (Fig. 2b). To verify the Janus structure, we compared these results with several MoS$_x$Se$_y$ monolayer samples with a randomized S and Se distribution[13]. The percentage of Se is derived from the X-ray photoelectron spectroscopy peak intensity and corrected by a relative sensitivity factor[17] for each atom (Se$_{XPS}$% = N(Se)/[N(Se) + N(S)], see Supplementary Information and Supplementary Table 5 for details), should be independent of the X-ray photon energy if the sample is vertically homogeneous in composition, as shown in Fig. 2c. The value of Se$_{XPS}$% for the Janus MoSSe monolayer is plotted as black circles in Fig. 2d, where the strong energy dependence indicates structural inhomogeneity in the vertical directions. This energy dependence can be understood as follows. Assuming that the electron intensity I_0 emitted from the bottom S layer is attenuated according to the Beer–Lambert law, the intensity reaching the surface will be $I = I_0 \exp(-d/L(E))$[18], where $L(E)$ is an energy-dependent electron attenuation length and d is the separation between the bottom S layers and the surface Se layers predicted by density functional theory calculations in Fig. 2a. This will introduce an energy dependence in Se$_{XPS}$% for the Janus MoSSe monolayer, as discussed in the Supplementary Materials. A plot of the best fit of the calculated Se percentage is compared with the experimental data in Fig. 2d.

The asymmetry in the chemical bonding within monolayers can be revealed by optical second harmonic generation (SHG)[19]. In a
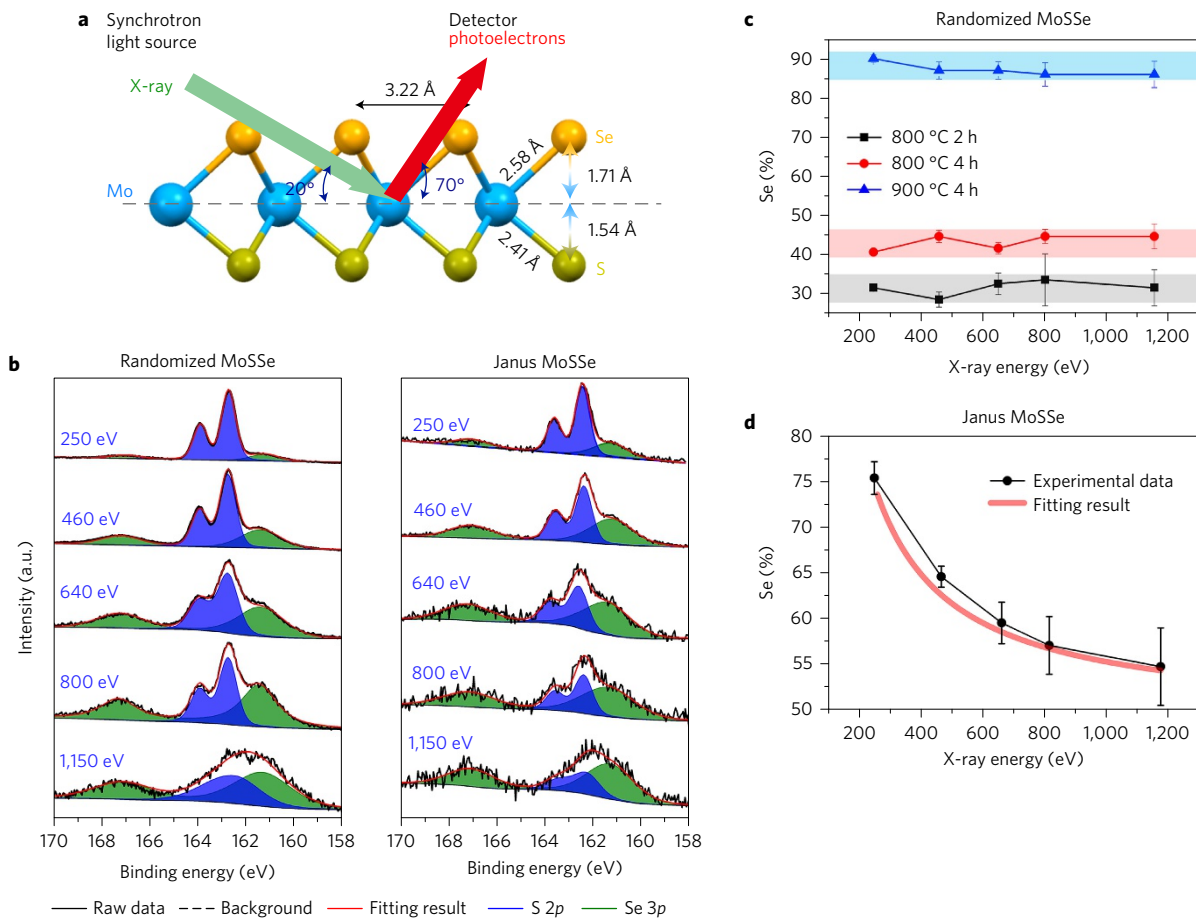
Figure 2 | Energy-dependent X-ray photoelectron spectroscopy. a, The incident angle is set to 20°. The molecular model is optimized by density functional theory calculations. **b**, Energy-dependent X-ray photoelectron spectra for Janus and randomized MoSSe monolayers. **c**, Dependence of Se_{XPS}% on photon energy for the randomized MoSSe monolayer. There is no obvious energy dependence. Various annealing conditions result in samples with different Se percentages. **d**, Dependence of Se_{XPS}% on photon energy for the Janus MoSSe monolayer, extracted based on the X-ray photoelectron spectroscopy results in **b** (and Supplementary Information). The real Se_{XPS}% on the top layer is 96.2%, as determined by energy-dispersive X-ray spectroscopy. Theoretical fitting results were calculated using the effective electron attenuation length (L_{EAL}) for two-dimensional materials (based on an equation provided in Supplementary Section 'Energy-dependent X-ray photoelectron spectroscopy'). Error bars indicate ±1 standard deviation.

Janus MoSSe monolayer, the imbalance of the electronic wave-function over the S and Se atom results in an out-of-plane optical dipole transition. To observe such an influence, we performed angle-resolved polarization-selective SHG measurements (Fig. 3a and Supplementary Fig. 9). First, the *p*-polarized fundamental light excites the sample under normal incidence, and *p*-polarized SHG signal I_p is collected. Because of the C_{3v} crystalline symmetry, the SHG induced by the in-plane dipole can be extinguished by rotating the crystal in-plane with the Mo–X bond direction perpendicular to the electric field[20,21]. To drive the out-of-plane dipole, a vertical electric field in a tilted incident beam is generated by positioning the scanning beam off-centre at the back aperture of the microscope objective. Because the projected *z*-component of the field increases as the tilt angle increases, the SHG intensity is expected to increase in the Janus MoSSe (Supplementary Fig. 10). In contrast, SHG from a randomized MoSSe alloy without the out-of-plane dipole should be insensitive to the increasing *z*-component electrical field. Note that the trend for the absolute SHG intensity not only includes information from the out-of-plane dipole, but is also affected by the system's angle (or position)-dependent collection efficiency. To exclude such extrinsic factors, the *s*-polarized SHG I_s induced by the in-plane dipole with the same collection efficiency is measured, and the ratio I_p/I_s is used to evaluate the intrinsic dipole contribution.

Figure 3b plots the angle-dependent SHG ratio I_p/I_s from Janus and randomized MoSSe monolayers. The SHG of the Janus sample strongly depends on the incident angle, while that from the alloy sample shows almost no change. In addition, the response is symmetric for positive and negative tilt angle incidences. This observation confirms the presence of an out-of-plane dipole in the MoSSe monolayers. To extract the second-order susceptibility associated with the out-of-plane dipole, the data were fitted by an angle-dependent SHG model (Supplementary Fig. 11 and Supplementary Information). The well-matched fitting confirms that second-order susceptibilities $\chi^{(2)}_{xxz}$, $\chi^{(2)}_{xzx}$ and $\chi^{(2)}_{zxx}$ play a role and indicate a magnitude ratio $\chi^{(2)}_{yxx}$:$\chi^{(2)}_{xxz}$ of 10:1 at 1,080 nm pump. To statistically confirm the vertical dipole SHG response, we measured five MoSSe Janus samples and three MoSSe alloy samples, whose second-order susceptibilities are summarized in Fig. 3c. For all asymmetric samples, the out-of-plane dipole generates observable $\chi^{(2)}_{xxz}$, $\chi^{(2)}_{xzx}$ and $\chi^{(2)}_{zxx}$, with little variation, whereas for all randomized samples, the out-of-plane dipole response is almost one order of magnitude smaller and within measurement limits. Note that our simulations for the in-plane and out-of-plane second-order susceptibilities for the MoSSe monolayer do show anisotropic features (Supplementary Fig. 12).

As a result of the out-of-plane asymmetry, Janus MoSSe experimentally shows an intrinsic vertical piezoelectric response, the
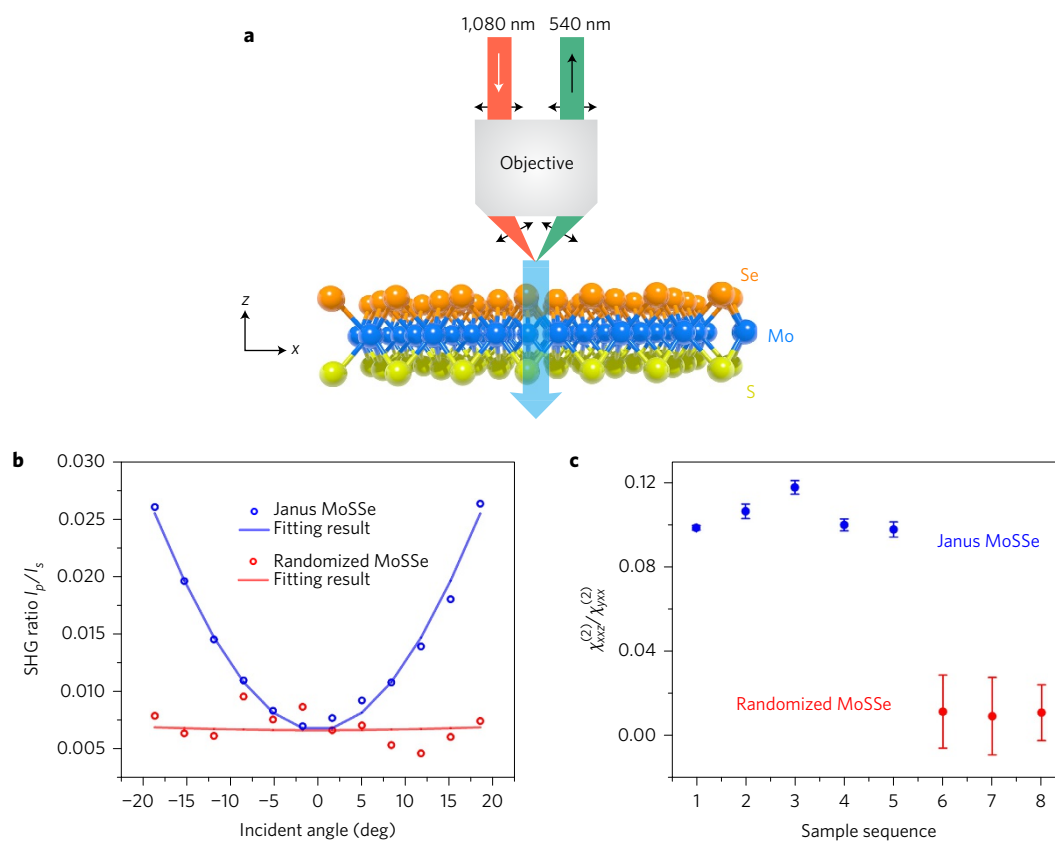
Figure 3 | Out-of-plane dipole probed by angle-resolved SHG. a, Schematics of out-of-plane induced SHG. A collimated p-polarized (along the x direction) pump beam with 1 mm spot size is guided to the objective back aperture (D = 7.6 mm). The beam (red) is focused at the sample with a tilted angle and generates an oscillating vertical electrical field to drive the out-of-plane dipole (blue arrow) for SHG. The SHG (green) is collected by the same objective and analysed by a polarizer. The beam position at the objective back aperture can be scanned along the x direction with a motorized stage, which tunes the incident angle accordingly. **b**, Angle-dependent SHG intensity ratio between p and s polarization in the Janus MoSSe and randomized alloy samples. In the Janus MoSSe sample, the I_p/I_s ratio (blue circles) increases symmetrically with more tilted incidence, and is fitted well by an angle-dependent SHG model (blue curve; see Supplementary Section 'Second-harmonic generation' for model details). In the MoSSe alloy, the I_p/I_s ratio (red circles) undergoes almost no change as the incident angle varies, and the flat fitting (red curve) suggests a negligible out-of-plane dipole. **c**, Second-order susceptibility ratio statistics. Five Janus MoSSe samples show a consistent out-of-plane and in-plane second-order susceptibility ratio (1:10); in contrast, three MoSSe alloy samples show a one order of magnitude smaller ratio. The error bars represent fitting error.

first demonstration in a single-molecular-layer crystal[22,23]. Because the distortion of Mo–S and Mo–Se bonds under an electric field do not cancel, a net thickness change is induced by applying a vertical voltage. To measure this out-of-plane deformation of this subnanometre layer, we used piezoresponse force microscopy, with resonance enhancement to boost the sensitivity by two orders of magnitude (Supplementary Figs 13 and 14)[24,25]. Optimized surface quality and electrical back contacts are achieved by synthesizing Janus MoSSe directly on atomically flat conductive substrates (highly oriented pyrolytic graphite, HOPG). As a result, we observe a clear piezoelectric contrast between the Janus MoSSe monolayer and the substrate (Fig. 4a,b and Supplementary Fig. 16). A sufficient signal-to-background ratio is only possible after balancing the potential of the tip and the substrate to minimize the electrostatic effect (Supplementary Fig. 15)[26]. This contrast cannot come from topographic, mechanical or electrochemical artefacts, because the randomized alloy monolayer does not provide visible contrast under the same experimental condition (Supplementary Fig. 17).

While most as-grown monolayers are topographically uniform, we obtained additional insight on those flakes carrying back-folding areas comprising a bilayer and a hole, created by thermal expansion mismatch. Because the vertical polarization of each layer is opposite in bilayers, the total piezoelectricity of the bilayer region should be suppressed[27]. This 'more is less' effect is

highlighted in a parallel comparison of the cross-sections (Fig. 4c), where a peak in height always corresponds to a dip in piezoelectric amplitude. Such a strong correlation (Supplementary Fig. 18) further verifies that the piezoresponse force microscopy contrast comes from piezoelectricity with a structural symmetry origin. The corresponding piezoelectric coefficient d_{33} is ~0.1 pm V^{-1} and can potentially be improved by one order of magnitude by increasing the dipolar contrast of the chemical bonds. Meanwhile, we caution that the value is qualitative, because the effective piezoelectricity of semiconducting MoSSe can be sensitive to a variation in electrical properties, as the cross-section also suggests some non-uniformity of the piezoresponse within the monolayer region[28].

In summary, the presented synthetic strategy achieves asymmetric transition metal dichalcogenide monolayers with symmetry breaking in the out-of-plane direction. The optically active vertical dipole provides a two-dimensional platform to study light–matter interactions where dipole orientation is critical, such as dipole–dipole correlations and strong coupling with plasmonic structures[29]. The out-of-plane piezoelectricity in two-dimensional monolayers brings an additional degree of freedom to the design and motion control of practical nanoelectromechanical devices[30]. Moreover, this polar monolayer with enhanced Rashba spin–orbit interaction sets an important milestone for future spintronics[9,31].

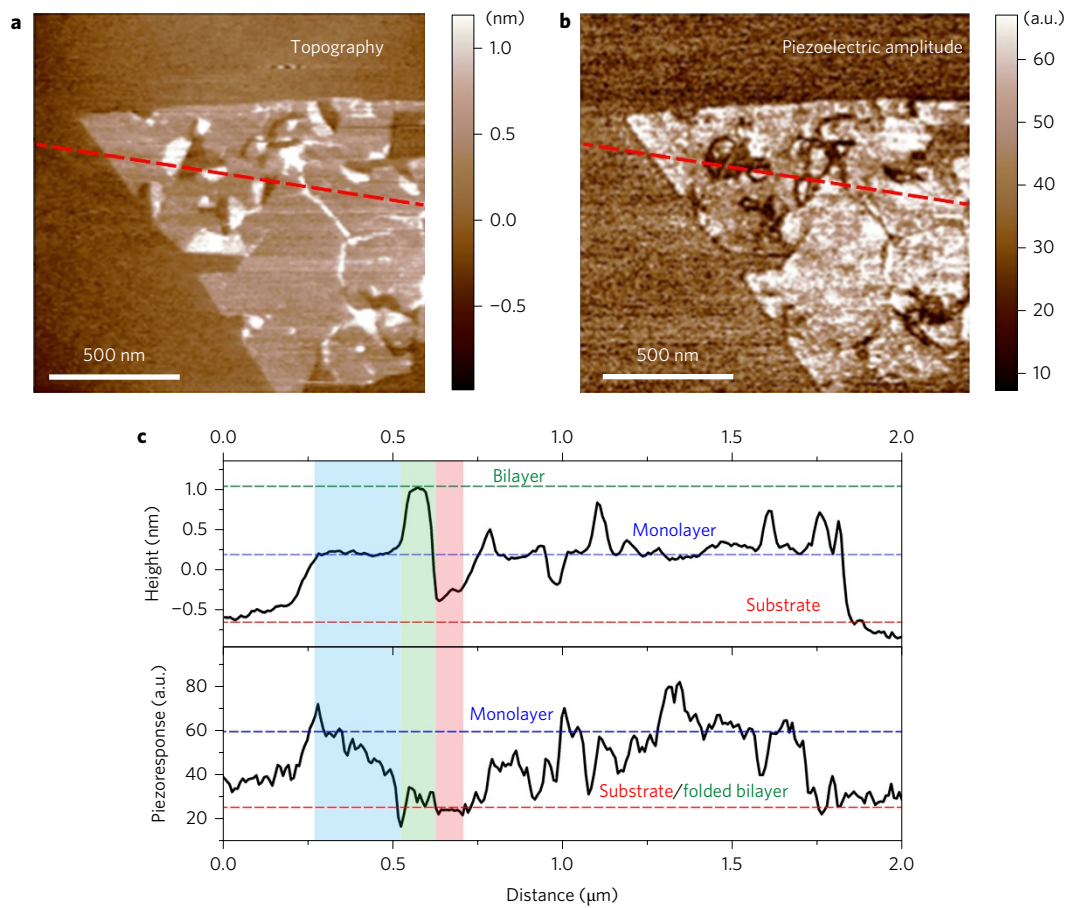**Figure 4 | Characterization of out-of-plane piezoelectricity in the Janus MoSSe monolayer. a,b,** Topography (**a**) and piezoelectric amplitude (**b**) of an isolated Janus MoSSe monolayer directly grown on HOPG, measured by resonance-enhanced piezoresponse force microscopy. The layer is uniform in most areas, and shows clear piezoelectric contrast, except for some broken and folded regions that give almost the same response as the substrate. Scale bars, 500 nm. **c,** For parallel comparison, cross-sections along the dashed lines in both images are compared. From the height (0.7 nm per step) we can unambiguously identify the region of the substrate: Janus monolayer or backfolded bilayer. The different piezoelectric amplitude levels of the Janus MoSSe monolayer and the substrate are also indicated, from which we estimate an out-of-plane piezoelectric coefficient of ~0.1 pm V^{-1}. Because the backfolded region contains two layers with opposite polarity, it has weaker piezoelectricity, proving the symmetry origin of the observed contrast and ruling out topographic or interfacial effects. The uncertainty primarily comes from spatial variation.

Methods

Methods and any associated references are available in the online version of the paper.

References

1. Zhang, Y. *et al.* Direct observation of a widely tunable bandgap in bilayer graphene. *Nature* **459,** 820–823 (2009).
2. Shimazaki, Y. *et al.* Generation and detection of pure valley current by electrically induced Berry curvature in bilayer graphene. *Nat. Phys.* **11,** 1032–1036 (2015).
3. Hunt, B. *et al.* Massive Dirac fermions and Hofstadter butterfly in a van der Waals heterostructure. *Science* **340,** 1427–1430 (2013).
4. Ponomarenko, L. A. *et al.* Cloning of Dirac fermions in graphene superlattices. *Nature* **497,** 594–597 (2013).
5. Ye, Z. *et al.* Probing excitonic dark states in single-layer tungsten disulphide. *Nature* **513,** 214–218 (2014).
6. Mak, K. F. & Shan, J. Photonics and optoelectronics of 2D semiconductor transition metal dichalcogenides. *Nat. Photon.* **10,** 216–226 (2016).
7. Yuan, H. *et al.* Zeeman-type spin splitting controlled by an electric field. *Nat. Phys.* **9,** 563–569 (2013).
8. Wu, S. *et al.* Electrical tuning of valley magnetic moment through symmetry control in bilayer MoS$_2$. *Nat. Phys.* **9,** 149–153 (2013).
9. Cheng, Y. C., Zhu, Z. Y., Tahir, M. & Schwingenschlögl, U. Spin–orbit-induced spin splittings in polar transition metal dichalcogenide monolayers. *Europhys. Lett.* **102,** 57001 (2013).
10. Lee, Y.-H. *et al.* Synthesis of large-area MoS$_2$ atomic layers with chemical vapor deposition. *Adv. Mater.* **24,** 2320–2325 (2012).
11. Shi, Y., Li, H. & Li, L.-J. Recent advances in controlled synthesis of two-dimensional transition metal dichalcogenides via vapour deposition techniques. *Chem. Soc. Rev.* **44,** 2744–2756 (2015).
12. Liu, Y. *et al.* Layer-by-layer thinning of MoS$_2$ by plasma. *ACS Nano* **7,** 4202–4209 (2013).
13. Su, S.-H. *et al.* Band gap-tunable molybdenum sulfide selenide monolayer alloy. *Small* **10,** 2589–2594 (2014).
14. Li, H. *et al.* Lateral growth of composition graded atomic layer MoS$_{2(1-x)}$Se$_{2x}$ nanosheets. *J. Am. Chem. Soc.* **137,** 5284–5287 (2015).
15. Mak, K. F., He, K., Shan, J. & Heinz, T. F. Control of valley polarization in monolayer MoS$_2$ by optical helicity. *Nat. Nanotech.* **7,** 494–498 (2012).
16. Zeng, H., Dai, J., Yao, W., Xiao, D. & Cui, X. Valley polarization in MoS$_2$ monolayers by optical pumping. *Nat. Nanotech.* **7,** 490–493 (2012).
17. Yeh, J. J. & Lindau, I. Atomic subshell photoionization cross sections and asymmetry parameters: 1≤Z≤103. *At. Data Nucl. Data Tables* **32,** 1–155 (1985).
18. Seah, M. P. Simple universal curve for the energy-dependent electron attenuation length for all materials. *Surf. Interface Anal.* **44,** 1353–1359 (2012).
19. Corn, R. M. & Higgins, D. A. Optical second harmonic generation as a probe of surface chemistry. *Chem. Rev.* **94,** 107–125 (1994).
20. Kumar, N. *et al.* Second harmonic microscopy of monolayer MoS$_2$. *Phys. Rev. B* **87,** 161403 (2013).
21. Yin, X. *et al.* Edge nonlinear optics on a MoS$_2$ atomic monolayer. *Science* **344,** 488–490 (2014).
22. Bune, A. V. *et al.* Two-dimensional ferroelectric films. *Nature* **391,** 874–877 (1998).
23. da Cunha Rodrigues, G. *et al.* Strong piezoelectricity in single-layer graphene deposited on SiO$_2$ grating substrates. *Nat. Commun.* **6,** 7572 (2015).

24. Rodriguez, B. J., Callahan, C., Kalinin, S. V. & Proksch, R. Dual-frequency resonance-tracking atomic force microscopy. *Nanotechnology* **18,** 475504 (2007).
25. Hong, S. *et al.* High resolution study of domain nucleation and growth during polarization switching in Pb(Zr,Ti)O₃ ferroelectric thin film capacitors. *J. Appl. Phys.* **86,** 607–613 (1999).
26. Johann, F., Hoffmann, Á. & Soergel, E. Impact of electrostatic forces in contact-mode scanning force microscopy. *Phys. Rev. B* **81,** 094109 (2010).
27. Becher, C. *et al.* Functional ferroic heterostructures with tunable integral symmetry. *Nat. Commun.* **5,** 4295 (2014).
28. Wang, X. B. *et al.* The influence of different doping elements on microstructure, piezoelectric coefficient and resistivity of sputtered ZnO film. *Appl. Surf. Sci.* **253,** 1639–1643 (2006).
29. Akselrod, G. M. *et al.* Probing the mechanisms of large Purcell enhancement in plasmonic nanoantennas. *Nat. Photon.* **8,** 835–840 (2014).
30. Zhu, H. *et al.* Observation of piezoelectricity in free-standing monolayer MoS₂. *Nat. Nanotech.* **10,** 151–155 (2015).
31. Manchon, A., Koo, H. C., Nitta, J., Frolov, S. M. & Duine, R. A. New perspectives for Rashba spin–orbit coupling. *Nat. Mater.* **14,** 871–882 (2015).

Author contributions

A.-Y.L., H.Z. and J.X. contributed equally to this work. L.J.L., A.-Y.L. and X.Z. conceived the concept. C.-P.C. and M.-Y.C. provided theoretical support. A.-Y.L., C.-C.C. and C.-W.Y. performed the synthesis. M.-H.C., A.-Y.L., S.D. and D.N. ran the X-ray photoelectron spectroscopy experiments and analysed the results. H.Z. and Y.Y. measured the piezoresponses, supervised by P.Y. Y.H. performed the transmission electron microscopy measurements and analysis, supervised by D.A.M. J.X. ran the SHG experiments and analysed the results. A.-Y.L., H.Z., J.X., C.-P.C, M.-Y.C., L.-J.L. and X.Z. wrote the manuscript. All co-authors discussed the results and commented on the manuscript at all stages.

Additional information

Supplementary information is available in the online version of the paper. Reprints and permissions information is available online at www.nature.com/reprints. Publisher's note: Springer Nature remains neutral with regard to jurisdictional claims in published maps and institutional affiliations. Correspondence and requests for materials should be addressed to X.Z. and L.J.L.

Competing financial interests

The authors declare no competing financial interests.

Methods

Chemical vapour deposition synthesis and characterization of the MoSSe monolayer. We synthesized an asymmetric MoSSe monolayer using a home-made chemical vapour deposition system equipped with an inductively coupled plasma coil. As-grown MoS_2 was placed 10 cm downstream of the plasma coil inside a furnace tube, and the base pressure was pumped down to 1 mtorr at room temperature. Hydrogen plasma with a power of 50 W and a flow of 20 s.c.c.m. at a pressure of 100 mtorr was used for the sulfur stripping process, forming a MoSH monolayer. Without breaking vacuum, Se powder was evaporated at 240 °C using a heating belt to produce a thin Se layer coating on top of the MoSH. The furnace was heated to 450 °C with a heating rate of 20 °C min^{-1} in an Ar/H_2 mixed-gas flow (65:5 s.c.c.m.) environment and kept for 1 h for thermal sulfurization/selenization followed by slow cooling down to room temperature.

Characterizations of the MoSSe monolayer were performed by Raman spectroscopy (WITec alpha 300 confocal Raman microscope), atomic force microscopy (Cypher ES, Asylum Research Oxford Instruments), energy-dependent synchrotron X-ray photoelectron spectroscopy (at SLAC), energy-dispersive X-ray spectroscopy (FEI Titan ST, operated at 200 kV) and scanning transmission electron microscopy (FEI TITAN, operated at 120 kV with a probe current of ~10 pA).

SHG. A collimated p-polarized pulsed laser beam with 1 mm spot size was guided to the objective back aperture ($D = 7.6$ mm). The incident angle, determined by the beam position at the objective back aperture, was scanned by a motorized stage. The SHG was collected by the same objective and analysed by a polarizer. The sample was mounted on a rotation stage and rotated to a specific crystal angle, under normal incidence, to achieve in-plane dipole-induced SHG extinction along the p polarization.

Piezoresponse force microscopy. The piezoresponse of both the Janus and randomized MoSSe was measured under the same bias and force conditions with a dual a.c. resonance tracking piezoresponse force microscope (MFP-3D, Asylum Research). The a.c. amplitude was limited to 1.5 V to avoid electrical damage.

Data availability. The data that support the findings of this study are available from the corresponding authors upon reasonable request.